Promotion effects of alkali metals on iron molybdate catalysts for CO_2 catalytic hydrogenation

Zhou, Yong; Sadia Traore, Aliou; Peron, Deizi V.; Barrios, Alan J.; Chernyak, Sergei A.; Corda, Massimo; Safonova, Olga V.; Iulian Dugulan, Achim; Ersen, Ovidiu; More Authors

DOI
10.1016/j.jechem.2023.06.019

Publication date
2023

Document Version
Final published version

Published in
Journal of Energy Chemistry

Journal of Energy Chemistry 85 (2023) 291–300

Contents lists available at ScienceDirect

Journal of Energy Chemistry

journal homepage: www.elsevier.com/locate/jechem

http://www.journals.elsevier.com/journal-of-energy-chemistry/

Promotion effects of alkali metals on iron molybdate catalysts for CO_2 catalytic hydrogenation

Yong Zhou [a], Aliou Sadia Traore [b], Deizi V. Peron [a], Alan J. Barrios [a], Sergei A. Chernyak [a], Massimo Corda [a], Olga V. Safonova [c], Achim Iulian Dugulan [d], Ovidiu Ersen [b], Mirella Virginie [a], Vitaly V. Ordomsky [a,*], Andrei Y. Khodakov [a,*]

[a] University of Lille, CNRS, Centrale Lille, University of Artois, UMR 8181-UCCS-Unité de Catalyse et Chimie du Solide, Lille F-59000, France
[b] IPCMS, UMR 7504 CNRS, Université de Strasbourg, 23 rue du Loess, BP 43, Cedex 2, 67034 Strasbourg, France
[c] PSI, CH-5232 Villigen, Switzerland
[d] Fundamental Aspects of Materials and Energy Group, Delft University of Technology, Mekelweg 15, Delft 2629 JB, Netherlands

ARTICLE INFO

Article history:
Received 22 April 2023
Revised 8 June 2023
Accepted 15 June 2023
Available online 1 July 2023

Keywords:
CO_2 utilization
Iron molybdate catalysts
Promotion
Alkali metals
Light olefins
In-situ characterization

ABSTRACT

CO_2 hydrogenation is an attractive way to store and utilize carbon dioxide generated by industrial processes, as well as to produce valuable chemicals from renewable and abundant resources. Iron catalysts are commonly used for the hydrogenation of carbon oxides to hydrocarbons. Iron-molybdenum catalysts have found numerous applications in catalysis, but have been never evaluated in the CO_2 hydrogenation. In this work, the structural properties of iron-molybdenum catalysts without and with a promoting alkali metal (Li, Na, K, Rb, or Cs) were characterized using X-ray diffraction, hydrogen temperature-programmed reduction, CO_2 temperature-programmed desorption, in-situ ^{57}Fe Mossbauer spectroscopy and operando X-ray adsorption spectroscopy. Their catalytic performance was evaluated in the CO_2 hydrogenation. During the reaction conditions, the catalysts undergo the formation of an iron (II) molybdate structure, accompanied by a partial reduction of molybdenum and carbidization of iron. The rate of CO_2 conversion and product selectivity strongly depend on the promoting alkali metals, and electronegativity was identified as an important factor affecting the catalytic performance. Higher CO_2 conversion rates were observed with the promoters having higher electronegativity, while low electronegativity of alkali metals favors higher light olefin selectivity.

1. Introduction

The increase in the concentration of CO_2 in the atmosphere, one of the main greenhouse gases, is causing serious environmental problems such as global warming, ocean acidification and biodiversity crisis, etc [1–3]. This prompts us to take urgent actions to stabilize the concentration of CO_2 by reducing its emissions and developing effective technologies [4–6] to capture and utilize CO_2.

To date, among the available tools, catalytic hydrogenation of CO_2 to value-added products, especially light olefins, with high activity, selectivity, and stability is highly desirable for various applications [7] and represents a practical way to achieve carbon neutrality [8,9]. Along with extensive literature on optimized catalysts for Fischer-Tropsch synthesis (FTS) [10–13], iron- and cobalt-based catalysts are being tested for CO_2 hydrogenation. Compared to iron, cobalt catalysts preferably form methane in CO_2 hydrogenation [14,15]. To maximize the production of light olefins, more attention has to be paid to the optimization of catalyst composition and structure. Recent work [16] identified efficient promoters and elucidated structure-performance correlations in the CO_2 hydrogenation to light olefins over zirconia-supported iron catalysts. The strongest promoting effect has been observed on iron catalysts containing alkali metals and more particularly, potassium. A further increase in the light olefin selectivity could be realized by simultaneous promotion of iron catalysts with alkali metals and molybdenum [16].

The promotion of iron catalysts with alkali metals varies as a function of catalytic support. The electronic interaction of iron species and alkali may modify the intrinsic reaction rate and selectivity. Alkali ions could enhance carbon monoxide dissociation,

* Corresponding authors.
E-mail addresses: vitaly.ordomsky@univ-lille.fr (V.V. Ordomsky), andrei.khodakov@univ-lille.fr (A.Y. Khodakov).

https://doi.org/10.1016/j.jechem.2023.06.019

because of election-donation effect on the iron species from basic oxygen species. The promotion by alkali metals reduces catalyst hydrogenation and increases the olefin to paraffin ratio in the reaction products. The water gas shift (WGS) activity usually increases in the alkaline-promoted catalysts. The chain growth probability and selectivity to C_{5+} hydrocarbons are usually enhanced over alkaline-promoted iron catalysts.

Iron molybdates with a tunable Mo/Fe ratio are known for their high activity and stability, making them a popular choice for numerous catalytic applications. Some of the common reactions include the oxidation of benzene, water gas shift reaction [17], selective oxidation of methanol to formaldehyde [18,19], hydrogenation of alkenes, and dehydrogenation of alcohols. Iron molybdates can also play a role of precursors for obtaining highly dispersed iron species after activation. However, to the best of our knowledge, iron molybdates have never been used as catalysts for CO_2 hydrogenation.

The structure of iron catalysts often evolves during catalytic reactions [20,21], where different transformations of active phases have been discovered [22,23]. Therefore, in order to clarify the active sites and to improve the catalytic performance, it is critical to understand the catalyst structure and structural dynamics under the reaction conditions. In-situ/operando characterization of catalysts is a promising strategy for identifying the instantaneous structure and understanding the structure-property relationship of catalysts [24–27]. In-situ/operando characterization under industrially relevant reaction conditions generally represents a significant experimental challenge, because of typically used high temperature, high pressure and the presence of a large number of reaction products [20–22,28].

In this paper, we prepared a series of iron-molybdenum catalysts and evaluated the effects of alkali metals (Li, Na, K, Rb, or Cs) on tuning the physicochemical properties and CO_2 hydrogenation performances of iron molybdate catalysts. To reveal the structure-performance correlations, iron molybdates promoted with alkali metals were characterized using several methods (X-ray diffraction, temperature-programmed reduction and desorption, high resolution transmission electron microscopy). The catalyst phase and structure evolution during activation and reaction were explored by in-situ Mössbauer and operando X-ray absorption spectroscopy (XAS). The reaction rate and selectivity were strongly affected by alkaline promoters. A higher CO_2 reaction rate was favored on the catalysts with high-electronegative alkaline promoters (Li and Na), whereas higher light olefin selectivity was observed with weakly electronegative counterparts (K, Rb, Cs).

2. Experimental

2.1. Catalyst preparation

Iron (III) nitrate nonahydrate ($Fe(NO_3)_3{\cdot}9H_2O$, 99.99%), ammonium molybdate tetrahydrate ($(NH_4)_6Mo_7O_{24}{\cdot}4H_2O$, 99.98%), lithium nitrate ($LiNO_3$, 99.99%), sodium nitrate ($NaNO_3$, 99.0%), potassium nitrate (KNO_3, 99.0%), rubidium nitrate ($RbNO_3$, 99.7%) and cesium nitrate ($CsNO_3$, 99.99%) were purchased from Sigma-Aldrich and used as precursors to prepare bulk FeMo-based catalysts. The catalysts were prepared by adding a calculated amount of $Fe(NO_3)_3{\cdot}9H_2O$, $(NH_4)_6Mo_7O_{24}{\cdot}4H_2O$ and eventually respective alkali nitrate (10% wt. Fe, 15% wt. Mo and 2% wt. alkali metal) in a mortar, and grinding them until reaching a homogeneous mixture. Then, they were calcined at 500 °C for 6 h under static air with a ramp of 2 °C min^{-1}. The obtained catalysts are denoted as FeMoX (X = Li, Na, K, Rb, or Cs). The solvent-free preparation strategy, by grinding and then calcinating the precursor salts employed in our study has several advantages including the environmental concerns, energy consumption, safety, and economic cost, etc. Water and other kinds of solvents, and additives are not necessary.

2.2. Catalyst characterization

The catalyst chemical compositions were determined using an energy dispersive micro-X-ray fluorescence spectrometer-M4 TORNADO (Bruker). The sample was irradiated using a rhodium X-ray tube (50 kV/200 mA, 10 W). This X-ray source is equipped with a poly-capillary lens enabling excitation of an area of 200 μm. For each sample, 36 points (of 200 μm) were analyzed covering the entire sample surface. The detector was a silicon-drift-detector Si (Li) with <145 eV resolution at 100 000 cps (Mn K_α) and cooled with Peltier cooling (−20 °C). The measurement was done under a vacuum (20 mbar). Quantitative analysis was done using fundamental parameters (FP) (standardless). The quantification was made on the basis of the identified element. The catalyst crystal structure was characterized by X-ray powder diffraction (XRD) using a Bruker AXS D8 diffractometer with monochromatic Cu Kα radiation (λ = 0.1538 nm). The XRD patterns were collected with the 2θ range between 5° and 80°, using a step size of 0.02° and with an acquisition time of 0.5 s. The identification of crystalline phases present in the catalysts was carried out by comparison with the JCPDS standard software.

The catalyst basicity was determined by CO_2 temperature-programmed desorption (CO_2-TPD) on an AutoChem II 2920 apparatus (Micromeritics). Before the measurements, the samples were pre-treated at 500 °C in He for 1 h, cooled to 40 °C, and exposed to CO_2 for 30 min. The samples then were heated with a ramping rate of 10 °C min^{-1} to reach 700 °C in He flow. The CO_2 desorption was measured with a TCD detector.

The reducibility of the catalysts was evaluated by hydrogen temperature-programmed reduction (H_2-TPR) using an AutoChem II 2920 apparatus (Micromeritics). The samples (~0.05 g) were reduced in a flow of 5% H_2/Ar flow (50 mL min^{-1}) and heated to 1000 °C with a temperature ramp rate of 10 °C min^{-1}.

TEM and STEM analyses were carried out using a TEM JEOL 2100F operating at 200 kV and equipped with a spherical aberration corrector. STEM micrographs were acquired using a camera length of 12 cm and a probe size of 0.1 nm. Elemental analyses were carried out with an energy dispersive X-ray spectroscopy (EDX) probe and a silicon drift detector (SDD) with a sensor size of 60 mm^2.

The transmission ^{57}Fe Mössbauer spectra were collected at −153 °C with a sinusoidal velocity spectrometer using a ^{57}Co (Rh) source. The velocity calibration was carried out using an α-Fe foil at room temperature. The source and absorbing samples were kept at the same temperature during the measurements. The Mössbauer spectra were fitted using the Mosswinn 4.0 program [29]. The experiments were performed at pressures up to 10 bar, in a state-of-the-art high-pressure Mössbauer in-situ cell, which was recently developed at the Reactor Institute of Delft [30]. The high-pressure beryllium windows in this cell contained 0.08% Fe impurity, whose spectral contribution was fitted and removed from the final spectra.

The in-situ X-ray absorption spectra were recorded at the Super XAS beamline station of the Swiss Light Source (Villigen PSI, Switzerland). The beam was monochromatized by Si (111) crystal. Prior to the analysis, the catalyst diluted with carbon nanotube (weight ratio = 1/1) was packed between two layers of quartz wool within a quartz capillary (O.D. = 2 mm). The measurements were performed under the flow of 5% CO/N_2 (P = 1 bar) for activation and $H_2/CO_2/N_2$ = 9/3/3, P = 6 bar) for the CO_2 hydrogenation at temperatures ranging from ambient to 350 °C. After the measurements, all data were processed by a ProQEXAFS software [31].

2.3. Catalytic tests

The catalytic performances in the CO_2 hydrogenation reaction were measured in a fixed-bed reactor with a 2 mm internal diameter and a length of 15 cm. The lower end of the reactor tube was filled with inert SiC (size of 500 μm), where ~110 mg of fresh catalyst had been loaded into the reactor. The catalysts were activated in CO under atmospheric pressure with a heating ramp of 2 °C min^{-1} until reaching a reaction temperature of 350 °C and dwelling at that temperature for 10 h under the CO flow (10 mL min^{-1}). After the activation, the catalysts were cooled to 180 °C and a gas mixture composed of $H_2/CO_2/N_2$ with the flow rates of 12/4/1 mL min^{-1} respectively, was fed into the reactor. Nitrogen was used as an internal standard for the calculation of CO_2 conversion. After the flow rates and the pressure (P = 10 bar) have been stabilized, the temperature was increased to 350 °C with a heating ramp of 2 °C min^{-1} to start the reaction. For the analysis of reactant and reaction products, a Bruker GC450 chromatograph equipped with a TCD and an FID detector was used. Two columns were used: the first is a packed CTR-1 column connected to the TCD detector, and the second is an Rt-Q-PLOT capillary column connected to the FID detector. Iron time yields (FTY) were expressed as moles of CO_2 converted per gram of iron (determined from XRF analysis) per second.

3. Results and discussion

3.1. CO_2 hydrogenation over iron-molybdenum catalysts

Before the catalytic performance tests, the catalysts were first activated with CO. Then, they were exposed to the flow of CO_2 and hydrogen. The catalytic data of different iron molybdates are shown in Fig. 1, Figs. S1, S2 and Table 1. The CO_2 conversion over all the catalysts displays an induction period, which is possibly due to modification of the catalyst structure. The CO_2 conversion then reaches a relatively steady value. The non-promoted FeMo catalyst shows a CO_2 conversion of 16.8% and thus corresponds to an FTY of 45.1 $\mu mol_{CO2}\ g_{Fe}^{-1}\ s^{-1}$. The main product was CH_4 (88.5%) along with a very small amount of light olefins ($C_{2-4}^{=}$, selectivity of 2.6%). The reaction rate expressed as FTY of FeMoX (X = Li, Na, K, Rb, and Cs) was a function of alkali metal. The Li- and Na-modified catalysts showed higher catalytic activity than unpromoted FeMo. In contrast, under the same space velocity, iron catalysts doped with other alkali metals show similar CO_2 conversions of ~10%, which are lower than for the FeMo catalyst. Higher reaction rates were observed over the catalysts promoted with highly electronegative alkali metals (Li and Na), while the reaction rate drops as the electronegativity of the promoting metal decreases. The CO_2 hydrogenation rate over iron catalysts promoted with alkali metals is similar [15] to the promoted $CoCu/TiO_2$ catalyst, where the activity of Li-$CoCu/TiO_2$ outperformed other CoCu catalysts. The effect was attributed to the geometric effect of Li with a smaller ion radius on the active sites and its strong polarization ability [15], compared to other alkali metals.

Fig. S1(b–d) shows hydrocarbon selectivity over iron molybdates as a function of CO_2 conversion. The C_{2+} product selectivity (light olefins and C_{5+} products) at a similar CO_2 conversion of about 15%, increases in the order of Li < Na < K < Rb < Cs (Fig. 1d and Fig. S2). The increase in light olefin and C_{5+} hydrocarbon selectivities occurs at the expense of methane. Interestingly, compared to unpromoted FeMo, promotion with heavier alkali metals (K, Rb and Cs) increases the selectivity to light olefins by a factor of ~5.5. In particular, FeMoCs exhibits the lowest selectivity to CH_4 among the catalysts and remarkably higher selectivity to light olefins (29.7%) (Table 1). The methane selectivity seems to be more

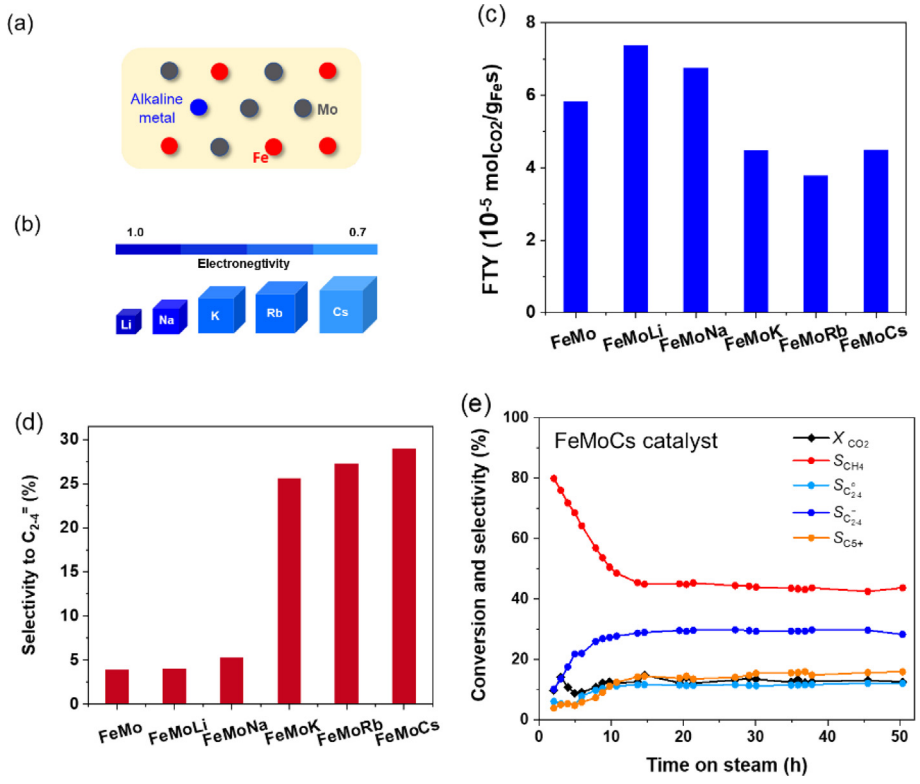

Fig. 1. CO_2 hydrogenation performances of iron molybdate catalysts ($H_2/CO_2/N_2$ = 12/4/1, 9300 mL $g_{catalyst}^{-1}\ h^{-1}$, 10 bar, 350 °C). (a) Scheme of the catalyst composition. (b) Pauling electronegativity of alkali metals. (c) Iron time yield (FTY, TOS = 22 h). (d) Light olefin selectivity ($S_{C2-4}^{=}$) at similar CO_2 conversion of ~15%. (e) CO_2 conversion (X_{CO2}) and hydrocarbons selectivity as a function of TOS over FeMoCs.

Table 1
CO_2 hydrogenation over iron molybdate catalysts (110 mg catalyst, $H_2/CO_2/N_2$ flow rates = 12/4/1 mL min^{-1}, 9300 mL $g_{catalyst}^{-1}$ h^{-1}, 10 bar, 350 °C, TOS = 22 h).

Catalyst	X_{CO2} (%)	FTY (μmol_{CO2} g_{Fe}^{-1} s^{-1})	S_{CO} (%)	CO-free product selectivity (%)			
				S_{CH4}	S^{o}_{C2-4}	$S^{=}_{C2-4}$	S_{C5+}
FeMo	16.8	45.1	52.9	88.5	8.5	2.6	0.3
FeMoLi	22.9	61.5	38.4	86.6	6.2	5.7	1.4
FeMoNa	22.2	59.6	47.8	79.7	6.4	11.9	2.0
FeMoK	13.9	37.3	53.8	58.1	4.5	31.1	6.3
FeMoRb	10.2	27.4	36.7	56.8	3.2	28.2	11.9
FeMoCs	12.1	32.5	41.0	45.3	11.5	29.7	13.6

related to the catalyst than to the reaction condition used. Note that the methane selectivity over iron catalysts is usually slightly affected by variation in the reaction pressure. Previously, the CO_2 hydrogenation was performed [28] over Fe catalysts at the temperature range of 280–340 °C, 30 bar and found the CH_4 selectivity is insensitive to the temperature variation and retained at about ~40%.

FeMoCs has been tested for a longer time on stream (TOS) of 50 h (Fig. 1e). After the stabilization for ~15 h, the CO_2 conversion was constant with an average value of ~13%. The selectivity to light olefins over FeMoCs reached ~29.8% under the steady-state conditions. We could conclude, that the alkali metals exert significant promoting effects on both CO_2 conversion and product selectivity. A higher CO_2 hydrogenation rate was observed over the catalysts with high electronegative promoters (Li and Na), while higher light olefin selectivity was detected on the catalysts containing less electronegative alkali metals (K, Rb, Cs) (Fig. 1).

3.2. Catalyst characterization

A wide range of characterization techniques were used to investigate the structure of iron catalysts. All the samples contain (Table S1) similar amounts of iron (7.3%–8.9%) and molybdenum (13.3%–15.5%). The XRD patterns of calcined, activated and spent iron molybdate catalysts are shown in Fig. 2. The patterns of calcined non-promoted FeMo and alkali metal promoted FeMoX catalysts (X = Li, Na, K, Rb and Cs) display diffraction peaks at 2θ of 13.8°, 15.3°, 19.4°, 20.4°, 22.9°, 25.1°, 25.7°, 27.5°, 30.1°, 31.4° and 34°, which correspond to the $Fe_2(MoO_4)_3$ phase (JCPDS 04-007-2787), while the peaks at 12.9° and 23.3° are attributed to orthorhombic α-MoO_3 (JCPDS 01-080-3491). No peaks attributed to iron oxides were detected in the calcined catalysts, probably because of their high dispersion. In addition, no diffraction peaks associated with the alkali metals are observed for all FeMoX samples, which may be due to their low concentrations.

The catalyst activation under carbon monoxide results in the modification of XRD patterns. In addition to the $Fe_2(MoO_4)_3$ and MoO_3 peaks, new diffraction peaks are observed at 13.1°, 26.3°, and 33.7°. They correspond to $FeMoO_4$ (JCPDS 00-022-0628). This new phase could be formed by the reduction of Fe^{3+} to Fe^{2+} species during the CO activation. The XRD patterns for the spent catalysts after the CO_2 hydrogenation were also recorded. Most of the diffraction peaks related to $Fe_2(MoO_4)_3$ and $FeMoO_4$ weaken or disappear after the reaction, while the spent catalysts exhibit diffraction peaks at 2θ angles around 42.9° that could be attributed [16] to iron carbides formed during the reaction.

High-resolution STEM and EDX elemental mapping were used to characterize FeMo and FeMoCs catalysts at different stages of

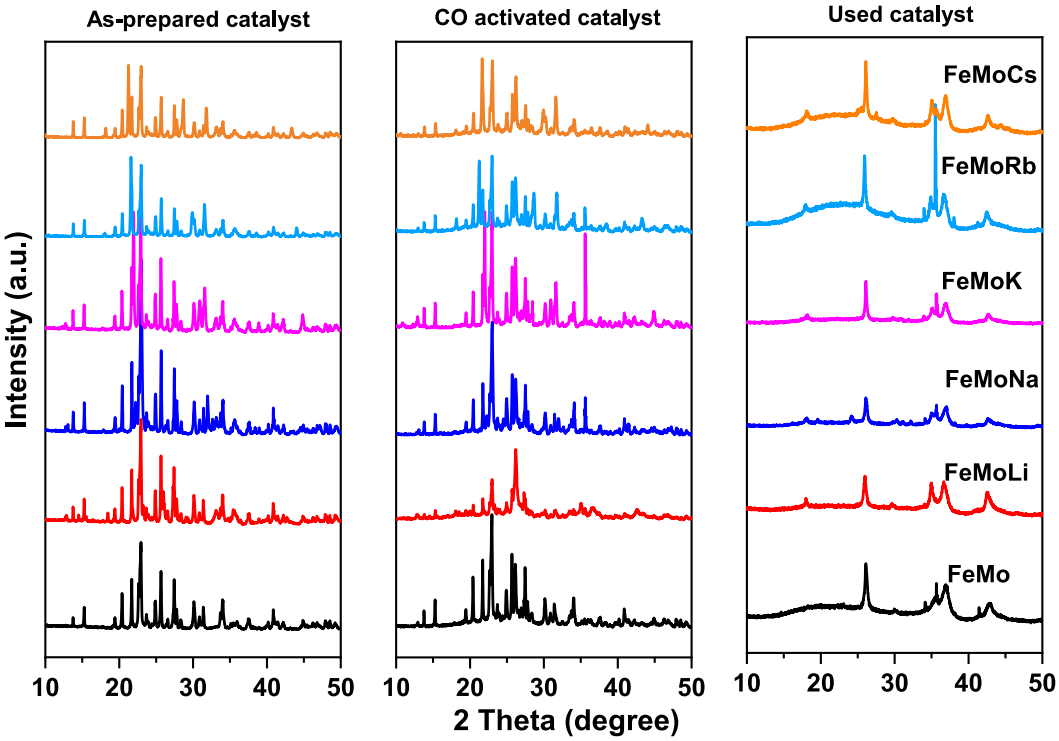

Fig. 2. XRD of as-prepared, CO activated, and used iron molybdate catalysts.

preparation, activation and reaction. The calcined FeMo is composed of oxide particles of around 15 nm (Fig. 3a and Fig. S3). Interestingly, after the CO activation, iron and molybdenum species became spatially separated. The segregation occurs during CO reduction and carbidization. However, these two components merge again during the CO_2 hydrogenation. In addition, carbon deposition was observed over the spent FeMo sample (Fig. S4). Remarkably, calcined FeMoCs showed domains with different compositions (Fig. 4 and Fig. S5), which are iron molybdates (marked as yellow circle), iron oxides (green square) and molybdenum oxides (blue square). This suggests that the alkali metals promote the phase separation during the calcination. Note that carbon is mainly deposited around the iron oxide particles for the spent catalyst. After the reaction, both catalysts almost retained the particle size. In contrast to FeMo, subsequent CO activation and reaction did not significantly change the morphology and phase composition of FeMoCs catalyst.

Previous reports suggest [16,32] that the surface basicity of catalysts may play an important role in the CO_2 hydrogenation. CO_2-TPD was used to investigate the surface basic properties of iron molybdate catalysts. Fig. 5 and Table S1 show a very low amount of adsorbed CO_2 (2.8 μmol g^{-1}) over unpromoted FeMo. The CO_2-TPD profile of FeMo displays only a broad peak located at 550–700 °C, which corresponds to the CO_2 desorption from the strong basic sites. Promotion with alkali metals leads to the appearance of weaker basic sites with TPD peaks at 300–500 °C, along with high temperature peaks. The catalysts promoted with alkali metals exhibit a higher quantity of desorbed CO_2 (3.4–6.1 vs. 2.8 μmol g^{-1} for the unpromoted counterpart). The total amount of basic sites increases in the following order of FeMoLi < FeMo < FeMoNa < FeMoK ≈ FeMoCs < FeMoRb. Interestingly, a fraction of weak acid sites (Table S1) was higher in the catalysts promoted with Li^+ and Na^+. Kondratenko [32] et.al proposed that too strong CO_2 adsorption is unfavorable for the catalyst activity. Following the trends between CO_2 transformation activity and surface basic properties of iron molybdate catalysts, we may conclude that more electronegative alkali metals such as Li and Na, which produce weak and moderate surface basicity in the iron molybdate catalysts, seem to facilitate the CO_2 activation and further the CO_2 hydrogenation activity.

The catalyst reducibility was evaluated by H_2-TPR (Fig. 6 and Table S1). No hydrogen consumption below 400 °C was observed for all the catalysts. Non-promoted FeMo showed three broad TPR peaks at 657, 800 and 962 °C. These peaks can be associated with the three step reduction of iron (III) molybdate: $Fe_2(MoO_4)_3 \rightarrow FeMoO_4 + Mo_4O_{11} \rightarrow Fe_2Mo_3O_8 + Fe_3O_4 \rightarrow$ Fe-Mo alloy [17,33]. This interpretation of H_2-TPR profiles is consistent with the previous report [17] for a bimetallic Fe-Mo/Al_2O_3 catalyst. The H_2-TPR profile of FeMoLi only slightly changes compared with that of FeMo. This suggests that Li has a weak effect on the reducibility of iron molybdate. In contrast, the promotion of iron molybdates with K, Rb and Cs shifts the dominant reduction peak to a lower temperature compared to FeMo (739–766 °C vs. 800 °C). This suggests that promotion with less electronegative promoters such as K, Rb and Cs enhances the catalyst reducibility.

In this work, the H_2-TPR tests were performed under a relatively diluted hydrogen (5% H_2/Ar). Although establishing direct correlations between the absolute temperature of TPR peaks and catalytic performance may be challenging, the catalysts with enhanced reducibility demonstrated an increased selectivity for C_{2+} hydrocarbons in CO_2 hydrogenation. Iron carbides are usually considered active species for CO hydrogenation over iron-based catalysts [34,35]. The increased reducibility of iron molybdates would allow more iron carbides to be produced during the catalyst activation and reaction.

3.3. Evolution of catalyst structure during activation and reaction

The evolution of catalyst structure of iron catalysts was investigated using in-situ Mössbauer spectrometry and operando XAS. The Mössbauer spectra were measured after the catalyst exposure to CO or reacting gas (CO during activation or H_2/CO_2 during the reaction) and then after rapid cooling to −153 °C (Fig. 7). The conditions used in the treatment of catalyst during the in-situ Mössbauer spectrometric measurements were similar to those in the catalytic tests. The Mössbauer spectra are displayed in Fig. 7. The Mössbauer fit parameters of calcined catalysts and catalyst exposed to CO and CO_2 + H_2 are given in Table 2.

The spectra of calcined samples reveal the presence of both hematite and $Fe_2(MoO_4)_3$ iron (III) molybdate phases (Table 2).

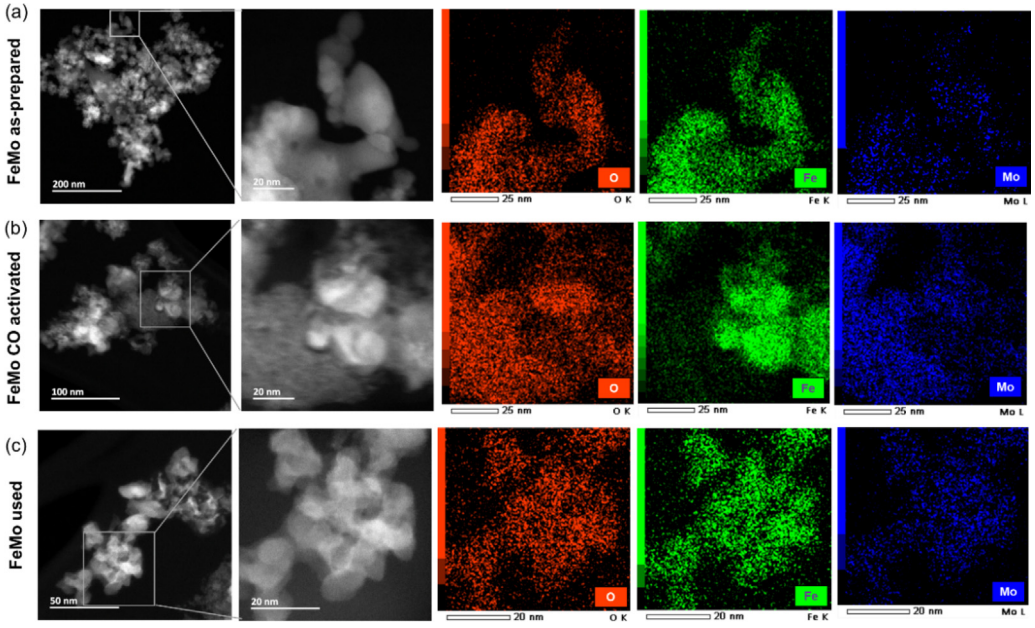

Fig. 3. STEM-ADF (annular dark field) and elemental mapping images of the calcined, activated, and spent FeMo (a, b, and c).

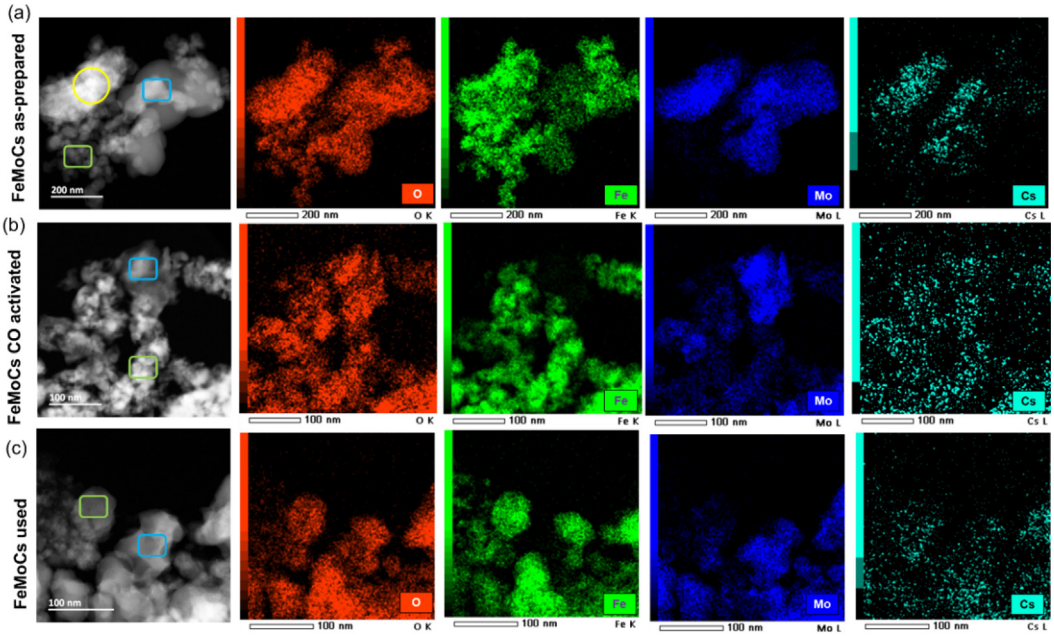

Fig. 4. STEM-ADF and elemental mapping images of the calcined, activated, and spent FeMoCs (a, b, and c).

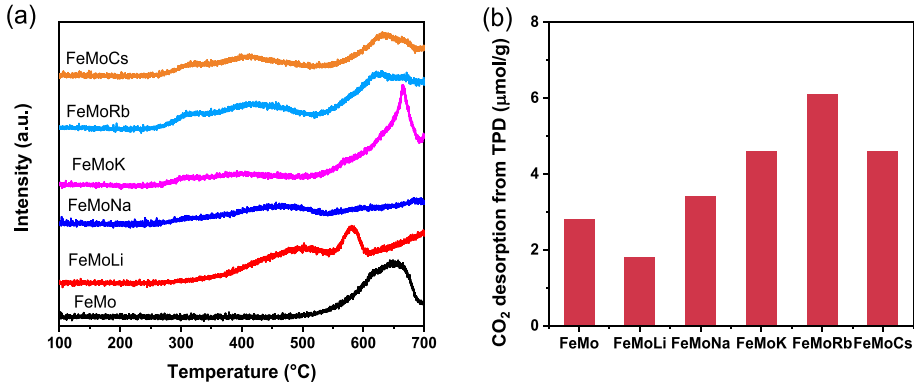

Fig. 5. CO_2-TPD profiles (a) and CO_2 desorption amount (b) measured over iron catalysts.

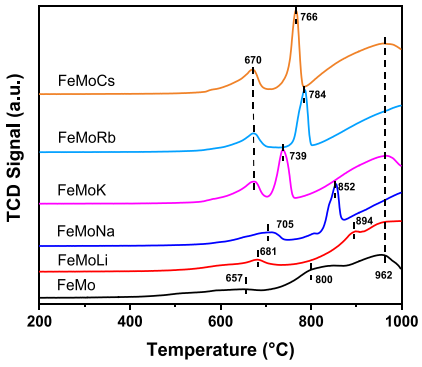

Fig. 6. H_2-TPR profiles of iron molybdate catalysts.

The Mossbauer results are consistent with the XRD data that also showed $Fe_2(MoO_4)_3$ as the main phase in the calcined catalysts. The weight ratio between hematite and ferric molybdate is different in FeMo and FeMoCs. The introduction of alkali metals increases the fraction of $Fe_2(Mo_3O)_4$ phase. In addition, the hematite hyperfine field is slightly smaller in FeMoCs compared to the FeMo sample, indicating Cs incorporation in the crystalline structure or better iron dispersion in FeMoCs.

Then, both FeMo and FeMoCs catalysts were in-situ activated in the CO flow (350 °C, 1 bar) and exposed to the reaction gas mixture (H_2/CO_2 = 3) at 350 °C and 10 bar. Note that the Mössbauer spectra of the catalysts during the activation and reaction are rather different from those of the calcined catalysts. After the CO activation, iron carbides and $FeMoO_4$ species were observed in both samples. These results indicate the partial reduction of $Fe_2(MoO_4)_3$ and carbidisation of iron oxide. Note that the total amount of iron carbides is comparable in FeMo and FeMoCs (23% vs. 19%).

After the activation in CO, the catalysts were exposed to H_2/CO_2 reacting mixture. Fig. 7 shows the in-situ Mössbauer spectra of catalysts measured during the reaction. In both catalysts, all the remaining $Fe_2(MoO_4)_3$ species were fully reduced to $FeMoO_4$ under the reaction gas. In addition, Fe-Mo alloy-like phase was formed. Remarkably, FeMoCs contains a larger amount of Fe-Mo alloy than the FeMo sample after the CO_2 hydrogenation (32% vs. 24%) (Table 2). Besides, the fraction of iron carbide slightly increases during the reaction. The Mössbauer results are therefore indicative of reduction of both molybdenum and iron during the catalyst activation and partial carbidization of iron. The reduction seems to be

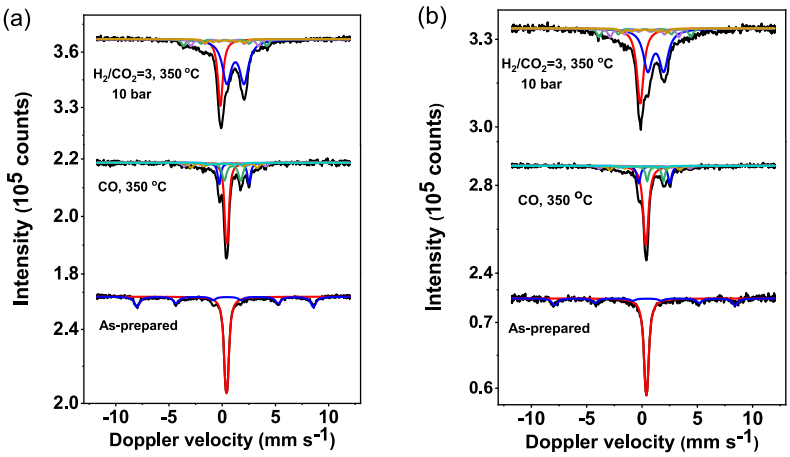

Fig. 7. In-situ Mössbauer spectra of FeMo (a) and FeMoCs (b) samples. The measurements were performed after rapid cooling to −153 °C (rouge $Fe_2(MoO_4)_3$, blue α-Fe_2O_3, green Fe-Mo).

Table 2
The Mössbauer fitted parameters of the iron catalysts, obtained at −153 °C*.

Sample/ Treatment	IS (mm s^{-1})	QS (mm s^{-1})	Hyperfine field (T)	Γ (mm s^{-1})	Phase	Spectral contribution (%)
FeMoAs-prepared	0.37	−0.17	51.5	0.59	α-Fe_2O_3	34
	0.40	0.19	-	0.41	$Fe_2(MoO_4)_3$	66
FeMoCO, 350 °C	0.26	-	23.7	0.46	χ-Fe_5C_2 (I)	8
	0.18	-	19.3	0.46	χ-Fe_5C_2 (II	11
	0.19	-	11.0	0.46	χ-Fe_5C_2 (III)	4
	0.43	0.19	-	0.35	$Fe_2(MoO_4)_3$	40
	1.12	2.79	-	0.34	β-$FeMoO_4$	17
	0.96	1.53	-	0.50	α-$FeMoO_4$	20
FeMoH_2/CO_2 = 3 350 °C, 10 bar	0.27	-	24.2	0.46	χ-Fe_5C_2 (I)	9
	0.22	-	19.7	0.46	χ-Fe_5C_2 (II)	9
	0.24	-	11.5	0.46	χ-Fe_5C_2 (III)	4
	−0.17	-	-	0.56	Fe-Mo	24
	1.24	1.62	-	1.00	α-$FeMoO_4$	54
FeMoCsAs-prepared	0.36	−0.20	50.7	0.59	α-Fe_2O_3	25
	0.40	0.15	-	0.45	$Fe_2(MoO_4)_3$	75
FeMoCsCO, 350 °C	0.25	-	25.3	0.47	χ-Fe_5C_2 (I)	6
	0.20	-	19.7	0.47	χ-Fe_5C_2 (II)	9
	0.16	-	12.2	0.47	χ-Fe_5C_2 (III)	4
	0.40	0.15	-	0.50	$Fe_2(MoO_4)_3$	53
	1.11	2.81	-	0.37	β-$FeMoO_4$	16
	1.20	1.46	-	0.34	α-FeMoO4	12
FeMoCs H_2/CO_2 = 3 350 °C, 10 bar	0.26	-	25.6	0.47	χ-Fe_5C_2 (I)	9
	0.21	-	19.3	0.47	χ-Fe_5C_2 (II)	9
	0.20	-	12.7	0.47	χ-Fe_5C_2 (III)	5
	−0.15	-	-	0.72	Fe-Mo	32
	1.24	1.44	-	0.98	α-$FeMoO_4$	45

* Experimental uncertainties: isomer shift: I.S. ± 0.02 mm s^{-1}; Quadrupole splitting: Q.S. ± 0.02 mm s^{-1}; line width: Γ ± 0.03 mm s^{-1}; hyperfine field: ± 0.1 T; spectral contribution: ± 3%.

enhanced in the presence of Cs and produces a higher fraction of Fe-Mo alloy. The in-situ Mössbauer results are consistent with the TPR profiles of FeMo and FeMoCs catalysts.

The evolution of the structure of FeMo and FeMoRb catalysts under the reaction conditions was further characterized by operando XAS. FeMoRb was chosen because of the possibility to measure the K absorption edges of Fe, Mo, and Rb under the same conditions [36].

First, we measured the Mo, Fe and Rb K-absorption edges of FeMo, FeMoRb and FeMoCs catalysts after calcination along with the spectra of several reference compounds (Figs. S6a and c, S7). The Mo K-edge position for calcined FeMo, FeMoRb and FeMoCs catalysts indicates mainly Mo^{6+} state. The XANES spectra (**Fig. S6**a) of all calcined catalysts also exhibit a pre-edge peak at around 19 995 eV, which is attributed to the dipole-forbidden/quadrupole-allowed 1 *s*–4*d* transition and is primarily associated with non-centrosymmetric tetrahedral geometry of Mo^{6+} in $Fe_2(MoO_4)_3$; for centrosymmetric Mo^{6+} in MoO_3 and Mo^{4+} in MoO_2 having octahedral coordination, this peak is much weaker or absent. Another peak at 20 015 eV is assigned to the dipole-allowed 1 *s*–5*p* transition, which is considered as characteristic feature of Mo species with a octahedral/distorted octahedral geometry [37].

Three iron samples show spectra similar to those of reference MoO_3 and $Fe_2(MoO_4)_3$, indicating that Mo in the catalysts possesses both tetrahedral and octahedral geometry. Their corresponding Fourier transform (FT) EXAFS moduli are shown in Fig. S6(b). In agreement with the literature, an intensive peak at 1.35 Å is assigned to the first shell Mo-O coordination [37], which suggests the presence of tetrahedral Mo-O species in $Fe_2(MoO_4)_3$.

In addition, the Fe K-edge XANES and Fourier transform (FT) EXAFS moduli of the calcined FeMo, FeMoRb and FeMoCs catalysts show similarity with reference $Fe_2(MoO_4)_3$ and Fe_2O_3. This suggests that iron in the calcined catalysts mainly presents as $Fe_2(MoO_4)_3$ and Fe_2O_3 phases. This observation agrees with the Mössbauer results. The XANES spectra of FeMoRb catalyst at the Rb K-absorption edge are displayed in Fig. S7. In the fresh calcined catalyst, rubidium is present as a mixture of rubidium hydroxide and carbonate. After conducting the CO_2 hydrogenation, Rb tends to agglomerate in rubidium oxide.

Fig. 8(b) shows that operando Mo K-edge XANES spectra of FeMoRb during CO activation and CO_2 hydrogenation show a gradual shift of edge position to lower energies, from around 20 008 to 20 002 eV. This shift indicates a continuous reduction of Mo in the presence of CO. Besides, the intensity of pre-edge peaks decreased and a peak around 20 015 eV increased simultaneously with the time. The spectrum evolution is indicative of the reduction of $Fe_2(MoO_4)_3$ and MoO_3 to $FeMoO_4$ and MoO_2. After the CO_2 hydrogenation, the pre-edge peak completely disappears and the XANES spectra get very similar to that of reference MoO_2. The Mo (VI) species seem to be completely reduced to Mo(IV) during the reaction. The corresponding FT Mo K-EXAFS moduli during the CO activation and CO_2 hydrogenation are shown in Fig. 8(c). During the CO activation and CO_2 hydrogenation, the intensity of the peak at 1.6 Å attributed to Mo-O tetrahedral coordination gradually decreases and completely disappears after the CO_2 hydrogenation.

Fig. 8(d and e) shows the operando Fe K-edge XANES and FT EXAFS spectra measured during CO activation and CO_2 hydrogenation. Initially, the Fe K-edge absorption edge was observed at 7132 eV. After the CO activation and CO_2 hydrogenation, the spectra exhibit a gradual shift towards lower energy indicating a change in the average oxidation state of Fe to a lower oxidation state, mainly corresponding to the formation of $FeMoO_4$ [37] and iron carbides.

The contributions of different phases obtained from liner combination fitting (LCF) analysis of the XANES spectra at the Mo and Fe K-edge during CO activation and CO_2 hydrogenation reaction are shown in Fig. 9 and Fig. S8. LCF was performed using standard spectra. $Fe_2(MoO_4)_3$, MoO_3, MoO_2 were used to fit the Mo K absorption edge, while the Fe K-edge was fitted using the reference spectra of $Fe_2(MoO_4)_3$, Fe_2O_3, FeO, and χ-Fe_5C_2. Fig. 9(a) shows that the Mo species started to reduce, when the temperature increased to 350 °C under CO, the fractions of MoO_3 and MoO_2 increased at the expense of $Fe_2(MoO_4)_3$. During the CO activation, the fraction of MoO_3 reaches a maximum and then decreases, while the quantity of MoO_2 kept increasing. The amount of these three Mo phases did not have significant variation during the CO_2 hydrogenation stage. Finally, after the reaction, the contributions from MoO_3 and MoO_2 were observed to be 23% and 77% respectively. LCF analysis (Fig. 9b) showed that the initial composition of the calcined FeMoRb was 66.1% $Fe_2(MoO_4)_3$ and 33.9% Fe_2O_3 which was similar to the Fe phases composition of the Mössbauer results obtained

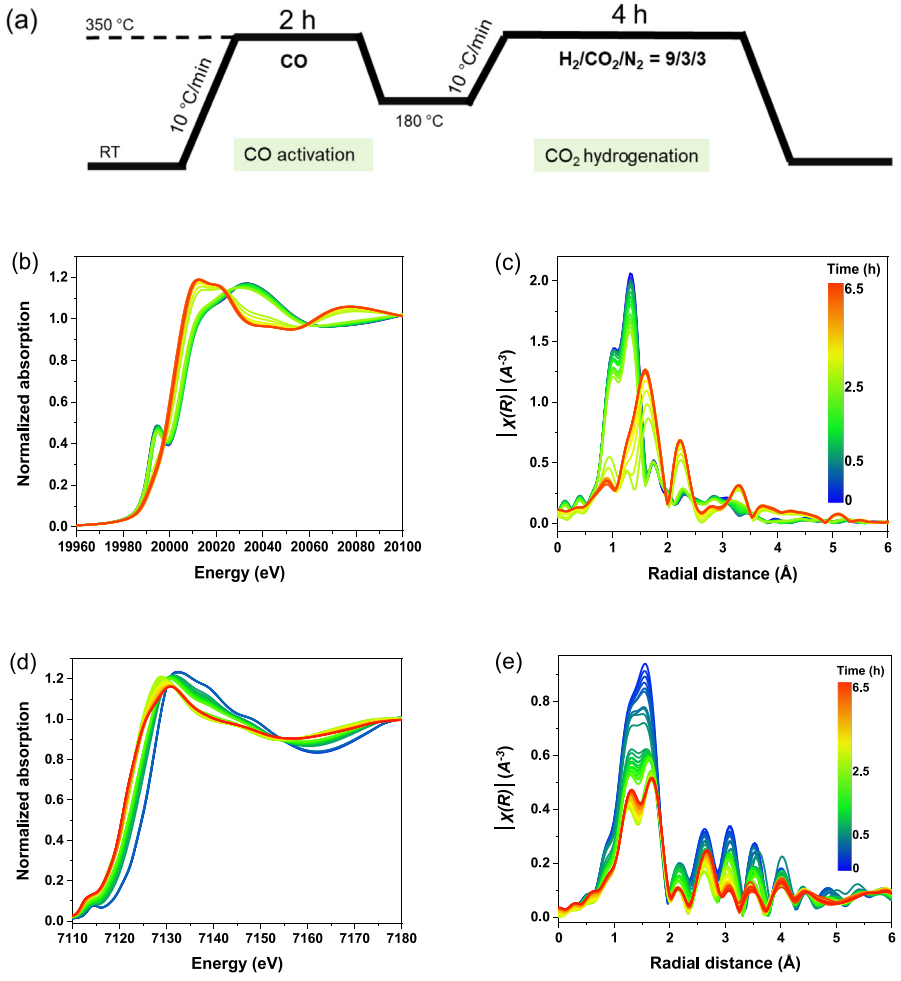

Fig. 8. (a) Procedures for in-situ XAS experiments. (b and d) In-situ Mo and Fe K-edge XANES spectra and (c and e) k^2-weighted Fourier transformed EXAFS spectra of FeMoRb catalyst during CO activation and CO_2 hydrogenation reaction.

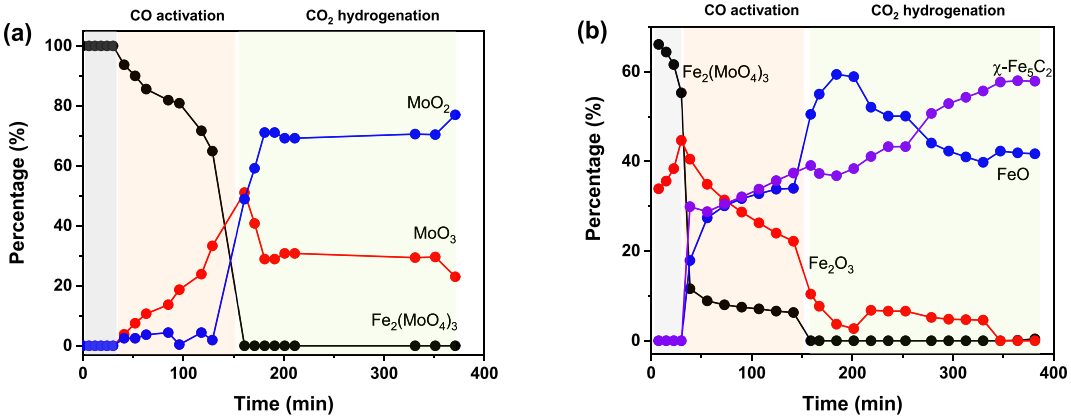

Fig. 9. Evolution of (a) Mo and(b) Fe phase compositions in FeMoRb during the CO activation and CO_2 hydrogenation reaction.

Table 3
Catalytic data of FeMoRb catalysts measured in in-situ XAS experiment (10 mg catalyst, $H_2/CO_2/N_2$ flow rates = 9/3/3 mL min^{-1}, 6 bar, 350 °C).

Experiment	TOS (min)	X_{CO2} (%)	S_{CO} (%)	CO-free product selectivity (%)			
				S_{CH4}	S_{C2-4}^{o}	$S_{C2-4}^{=}$	S_{C5}^{+}
Mo K-edge	46	8.0	97.6	78.7	8.2	7.4	5.8
	230	8.5	98.3	76.5	7.2	10.3	6.0
Fe K-edge	47	6.4	97.0	83.1	5.1	7.0	4.7
	235	7.1	97.9	78.2	5.9	8.4	7.5

from FeMoCs (75% $Fe_2(MoO_4)_3$, 25% Fe_2O_3). During the CO activation, both $Fe_2(MoO_4)_3$ and Fe_2O_3 contents decreased. The FeO phase appears as an intermediate in the carbidization of $Fe_2(MoO_4)_3$ and Fe_2O_3 to χ-Fe_5C_2 iron carbide. The addition of the contribution of iron metallic foil did not increase the fit quality.

The operando XAS spectra were measured simultaneously with chemical analysis of the reaction products (Table 3). The CO_2 conversion in the in-situ XAS cell leads to the production of CO and hydrocarbons. Different from the catalytic results obtained from the conventional fixed-bed set up, lower CO_2 conversion was observed in the in-situ XAS experiments with a much higher selectivity to CO. This discrepancy may be due to the lower reaction pressure and a shorter activation time of the catalyst in CO due to technical limitations in in-situ synchrotron experiments compared to traditional catalytic tests.

4. Conclusions

A series of iron-molybdenum catalysts promoted with alkali metals were prepared for CO_2 hydrogenation. The calcined catalysts contain iron (III) molybdate, MoO_3 and iron oxide species. The introduction of alkali metals results in a larger amount of basic sites. The presence of Cs and Rb increases the strength of basic sites and catalyst reducibility. Electronegativity of alkali metals seems to be a principal parameter of catalytic properties. Highly electronegative alkaline promoters favor CO_2 conversion rate, while the weakly electronegative alkali metals such as Cs and Rb result in catalysts with low reaction rates but higher light olefin selectivity. The in-situ/operando techniques employed in this work showed a gradual reduction of molybdenum and iron to $FeMoO_4$ and MoO_2 and FeO, respectively. The presence of Fe-Mo alloy was also detected. A part of iron is carbidized to iron carbides under catalyst activation and during the catalytic reaction.

Declaration of competing interest

The authors declare that they have no known competing financial interests or personal relationships that could have appeared to influence the work reported in this paper.

Acknowledgments

We thank Olivier Gardoll and Dr. Joelle Thuriot-Roukos for help in TPR-TPD and XRF characterizations. The authors acknowledge financial support from European Union (Interreg FWVL V project PSYCHE) and from the French National Research Agency (Multiprobe project, ANR-20-CE42-0007). We thank the Swiss Light Source and Super XAS beamline for the synchrotron measurements.

Appendix A. Supplementary data

Supplementary data to this article can be found online at https://doi.org/10.1016/j.jechem.2023.06.019.

References

[1] J.G. Canadell, C. Le Quéré, M.R. Raupach, C.B. Field, E.T. Buitenhuis, P. Ciais, T.J. Conway, N.P. Gillett, R. Houghton, G. Marland, Proc. Natl. Acad. Sci. U.S.A. 104 (2007) 18866–18870.
[2] O. Hoegh-Guldberg, P.J. Mumby, A.J. Hooten, R.S. Steneck, P. Greenfield, E. Gomez, C.D. Harvell, P.F. Sale, A.J. Edwards, K. Caldeira, Science 318 (2007) 1737–1742.
[3] F.E. Hopkins, P. Suntharalingam, M. Gehlen, O. Andrews, S.D. Archer, L. Bopp, E. Buitenhuis, I. Dadou, R. Duce, N. Goris, Proc. R. Soc. A 476 (2020) 20190769.
[4] W. Gao, S. Liang, R. Wang, Q. Jiang, Y. Zhang, Q. Zheng, B. Xie, C.Y. Toe, X. Zhu, J. Wang, Chem. Soc. Rev. 49 (2020) 8584–8686.
[5] Z. Zhang, S.Y. Pan, H. Li, J. Cai, A.G. Olabi, E.J. Anthony, V. Manovic, Renew. Sustain. Energy Rev. 125 (2020).
[6] F. Wang, J.D. Harindintwali, Z. Yuan, M. Wang, F. Wang, S. Li, Z. Yin, L. Huang, Y. Fu, L. Li, Innovation 2 (2021).
[7] S.C. Mandal, A. Das, D. Roy, S. Das, A.S. Nair, B. Pathak, Coord. Chem. Rev. 471 (2022).

[8] W. Zhang, Z. Jin, Z. Chen, Adv. Sci. 9 (2022) 2105204.
[9] S.A. Chernyak, M. Corda, J.P. Dath, V.V. Ordomsky, A.Y. Khodakov, Chem. Soc. Rev. 51 (2022) 7994–8044.
[10] B. Todić, V.V. Ordomsky, N.M. Nikačević, A.Y. Khodakov, D.B. Bukur, Catal. Sci. Technol. 5 (2015) 1400–1411.
[11] Z. Gholami, Z. Tišler, V. Rubáš, Catal. Rev. 63 (2021) 512–595.
[12] Y. Chen, J. Wei, M.S. Duyar, V.V. Ordomsky, A.Y. Khodakov, J. Liu, Chem. Soc. Rev. 50 (2021) 2337–2366.
[13] A.J. Barrios, B. Gu, Y. Luo, D.V. Peron, P.A. Chernavskii, M. Virginie, R. Wojcieszak, J.W. Thybaut, V.V. Ordomsky, A.Y. Khodakov, Appl. Catal. B: Environ. 273 (2020).
[14] Z. Shi, H. Yang, P. Gao, X. Li, L. Zhong, H. Wang, H. Liu, W. Wei, Y. Sun, Catal. Today 311 (2018) 65–73.
[15] Z. Shi, H. Yang, P. Gao, X. Chen, H. Liu, L. Zhong, H. Wang, W. Wei, Y. Sun, Chinese J. Catal. 39 (2018) 1294–1302.
[16] A.J. Barrios, D.V. Peron, A. Chakkingal, A.I. Dugulan, S. Moldovan, K. Nakouri, J. Thuriot-Roukos, R. Wojcieszak, J.W. Thybaut, M. Virginie, A.Y. Khodakov, ACS Catal. 12 (2022) 3211–3225.
[17] A.G. Kharaji, A. Shariati, M.A. Takassi, Chin. J. Chem. Eng. 21 (2013) 1007–1014.
[18] K. Routray, W. Zhou, C.J. Kiely, W. Grünert, I.E. Wachs, J. Catal. 275 (2010) 84–98.
[19] M.P. House, A.F. Carley, R. Echeverria-Valda, M. Bowker, J. Phys. Chem. C 112 (2008) 4333–4341.
[20] D.V. Peron, A.J. Barrios, A. Taschin, I. Dugulan, C. Marini, G. Gorni, S. Moldovan, S. Koneti, R. Wojcieszak, J.W. Thybaut, Appl. Catal. B: Environ. 292 (2021).
[21] B. Gu, D.V. Peron, A.J. Barrios, M. Bahri, O. Ersen, M. Vorokhta, B. Šmíd, D. Banerjee, M. Virginie, E. Marceau, R. Wojcieszak, V.V. Ordomsky, A.Y. Khodakov, Chem. Sci. 11 (2020) 6167–6182.
[22] K.F. Kalz, R. Kraehnert, M. Dvoyashkin, R. Dittmeyer, R. Gläser, U. Krewer, K. Reuter, J.D. Grunwaldt, ChemCatChem 9 (2017) 17–29.
[23] X. Zhang, S. Han, B. Zhu, G. Zhang, X. Li, Y. Gao, Z. Wu, B. Yang, Y. Liu, W. Baaziz, Nat. Catal. 3 (2020) 411–417.
[24] A.J. Foster, R.F. Lobo, Chem. Soc. Rev. 39 (2010) 4783–4793.
[25] X. Li, X. Yang, J. Zhang, Y. Huang, B. Liu, ACS Catal. 9 (2019) 2521–2531.
[26] J. Timoshenko, B. Roldan Cuenya, Chem. Rev. 121 (2020) 882–961.
[27] X. Li, S. Wang, L. Li, Y. Sun, Y. Xie, J. Am. Chem. Soc. 142 (2020) 9567–9581.
[28] J. Zhu, P. Wang, X. Zhang, G. Zhang, R. Li, W. Li, T.P. Senftle, W. Liu, J. Wang, Y. Wang, A. Zhang, Q. Fu, C. Song, X. Guo, Sci. Adv. 8 (2022), eabm3629.
[29] Z. Klencsar, Nucl. Instrum. Methods Phys. Res. B: Beam Interact. Mater. At. 129 (1997) 527–533.
[30] T.A. Wezendonk, V.P. Santos, M.A. Nasalevich, Q.S. Warringa, A.I. Dugulan, A. Chojecki, A.C. Koeken, M. Ruitenbeek, G. Meima, H.U. Islam, ACS Catal. 6 (2016) 3236–3247.
[31] A.H. Clark, J. Imbao, R. Frahm, M. Nachtegaal, J. Synchrotron Radiat. 27 (2020) 551–557.
[32] Q. Yang, V.A. Kondratenko, S.A. Petrov, D.E. Doronkin, E. Saraci, H. Lund, A. Arinchtein, R. Kraehnert, A.S. Skrypnik, A.A. Matvienko, E.V. Kondratenko, Angew. Chem. Int. Ed. 61 (2022) e202116517.
[33] H. Zhang, J. Shen, X. Ge, J. Solid State Chem. 117 (1995) 127–135.
[34] A.V. Puga, Catal. Sci. Technol. 8 (2018) 5681–5707.
[35] T. Herranz, S. Rojas, F.J. Pérez-Alonso, M. Ojeda, P. Terreros, J.L.G. Fierro, J. Catal. 243 (2006) 199–211.
[36] J.A. Bearden, A. Burr, Rev. Mod. Phys. 39 (1967) 125.
[37] A. Gaur, M. Stehle, K.V. Raun, J. Thrane, A.D. Jensen, J.D. Grunwaldt, M. Hoj, Phys. Chem. Chem. Phys. 22 (2020) 11713–11723.